



Full Length Article

Sensitive detection of SARS-CoV-2 spike protein based on electrochemical impedance spectroscopy of Fe₃O₄@SiO₂-Au/GCE biosensorXun-Hai You^{a,b,1}, Yao Liu^{a,c,1}, Yan-Yan Li^d, Bing Zhao^{a,b}, Yong Yang^d, Rohan Weerasooriya^{a,e}, Xing Chen^{a,b,c,e,*}^a Key Lab of Aerospace Structural Parts Forming Technology and Equipment of Anhui Province, Institute of Industry and Equipment Technology, Hefei University of Technology, Hefei 230009, PR China^b School of Materials Science and Engineering, Hefei University of Technology, Hefei 230009, PR China^c School of Resources and Environmental Engineering, Hefei University of Technology, Hefei 230009, PR China^d State Key Laboratory of High-Performance Ceramics and Superfine Microstructures, Shanghai Institute of Ceramics, Chinese Academy of Sciences, Shanghai 200050, PR China^e National Centre for Water Quality Research, National Institute of Fundamental Studies, Kandy, 20 000, Sri Lanka

ARTICLE INFO

Keywords:

SARS-CoV-2 spike protein
Fe₃O₄@SiO₂-Au nanocomposites
Electrochemical biosensor
Electrochemical impedance spectroscopy

ABSTRACT

Highly contagious COVID-19 disease is caused by a novel severe acute respiratory syndrome coronavirus 2 (SARS-CoV-2), which poses a serious threat to global public health. Therefore, the development of a fast and reliable method for the detection of SARS-CoV-2 is an urgent research need. The Fe₃O₄@SiO₂-Au is enriched with a variety of functional groups, which can be used to fabricate a sensitive electrochemical biosensor by bio-functionalization with angiotensin-converting enzyme 2 (ACE2). Accordingly, we developed a novel electrochemical sensor by chemically modifying a glassy carbon electrode (GCE) with Fe₃O₄@SiO₂-Au nanocomposites (hereafter Fe₃O₄@SiO₂-Au/GCE) for the rapid detection of S-protein spiked SARS-CoV-2 by electrochemical impedance spectroscopy (EIS). The new electrochemical sensor has a low limit detection (viz., 4.78 pg/mL) and a wide linear dynamic range (viz., 0.1 ng/mL to 10 μg/mL) for detecting the EIS response signal of S-protein. The robust Fe₃O₄@SiO₂-Au/GCE biosensor has high selectivity, stability, and reproducibility for the detection of S-protein with good recovery of saliva samples.

1. Introduction

Since the 21st century, three coronavirus outbreaks were reported at a global scale: severe acute respiratory syndrome (SARS) in 2002, Middle East respiratory syndrome (MERS) in 2012, and novel pneumonia caused by a coronavirus (SARS-CoV-2) in 2019 Corona Virus Disease 2019 (COVID-19) [1,2]. It is reported that the SARS-CoV-2 genome sequence is 77% and 50% homologous to SARS-CoV and MERS-CoV, respectively [3]. SARS-CoV-2 is more widespread compared to the other respiratory syndromes by spreading over two hundred countries causing 600 million infections and about 6 million deaths. Therefore, the development of a rapid and sensitive method for the detection of SARS-CoV-2 is urgently needed. Currently, virus detection methods rely on conventional laboratory techniques, including nucleic acid detection and serological

testing [4–6]. Among nucleic acid assay routes, the reverse transcription polymerase chain reaction (RT-PCR) is the core method for SARS-CoV-2 detection. However, RT-PCR-based methods require skilled personnel and specialized equipment [7]. Serological assays viz., including antigen and antibody assays, are based on antigen-antibody-specific binding assays [8,9]. There is a voluminous literature on the benefits of serological assays for SARS-CoV-2 detection, where antigen assays can only be used adjunct to detect SARS-CoV-2 [10]. Although these methods consume less time than RT-PCR measurements, they still have limitations due to arduous sample preparations and low sensitivity. Further the production of antibody assays requires SARS-CoV-2 infected patients for a period of 5–7 days. Previously, the development of electrochemical biosensors for medical diagnostic applications [11–13], including diabetes, Alzheimer's, and other diseases, have shown that they can be adapted as a

* Corresponding author. Key Lab of Aerospace Structural Parts Forming Technology and Equipment of Anhui Province, Institute of Industry and Equipment Technology, Hefei University of Technology, Hefei, 230009, PR China.

E-mail address: xingchen@hfut.edu.cn (X. Chen).

¹ These two authors contributed equally to these work.

<https://doi.org/10.1016/j.asems.2023.100067>

Received 4 May 2023; Received in revised form 23 May 2023; Accepted 24 May 2023

Available online 26 May 2023

2773-045X/© 2023 The Author(s). Published by Elsevier B.V. on behalf of Changchun Institute of Applied Chemistry, CAS. This is an open access article under the CC BY-NC-ND license (<http://creativecommons.org/licenses/by-nc-nd/4.0/>).

viral detection tool with high sensitivity, high specificity, low cost, and fast response time (Table S1). Notably, with the miniaturization and smart automation of electrochemical devices, these biosensors are also suited for clinical diagnosis and rapid detection of SARS-CoV-2 [14–16].

One of the key aspects of constructing electrochemical biosensors is the development of stable materials with desired conductivity and selectivity to an analyte [17,18]. There is a considerable literature on the development of different nanomaterials in electrochemical biosensors [19–22], including gold, carbon, metal oxide nanomaterials, etc. Fe_3O_4 nanoparticles attract attention in electrochemical sensor development particularly due to their biocompatibility, simple preparation, magnetic properties, high sorption capacity, and environmentally benign nature [23]. However, iron-derived substrates readily agglomerate and undergo rapid oxidation which limits their efficient use in sensor developments [24, 25]. To overcome these limitations and enhance stability, Fe_3O_4 nanoparticles are suitably compounded with carbon-derived substrates, metal oxides, and other metals, or polymers, etc. [23]. Presently, we developed a sensor by modifying glassy carbon electrode (GCE) with $\text{Fe}_3\text{O}_4@/\text{SiO}_2$ -Au nanocomposites to detect S-protein for SARS-CoV-2 diagnosis by electrochemical impedance spectroscopy (EIS). To facilitate electron transfer, minimize agglomeration, and retard undesired oxidation, the Fe_3O_4 nanoparticles were first coated with a thin SiO_2 layer and then doped with Au nanoparticles. To improve selectivity and sensitivity of SARS-CoV-2 detection, angiotensin-converting enzyme 2 (ACE2) was introduced to functionalize $\text{Fe}_3\text{O}_4@/\text{SiO}_2$ -Au composite to enhance S-protein binding ability [26–29]. This enables the rapid diagnosis of SARS-CoV-2 virus, which may open a new direction in COVID-19 research.

2. Materials and methods

2.1. Materials and apparatus

The SARS-CoV-2 S-protein and Fc-tag-tagged human ACE2 were obtained from Sino Biological (PR China). Analytical grade, ferric chloride hexahydrate ($\text{FeCl}_3 \cdot 6\text{H}_2\text{O}$), ethylene glycol ($\text{C}_2\text{H}_6\text{O}_2$), trisodium citrate dihydrate ($\text{C}_6\text{H}_5\text{Na}_3\text{O}_7 \cdot 2\text{H}_2\text{O}$), sodium acetate anhydrous (CH_3COONa), tetraethyl orthosilicate (TEOS), ammonia, 3-aminopropyl-triethoxysilane (APTES), chloroauric acid ($\text{HAuCl}_4 \cdot 4\text{H}_2\text{O}$), ethanol, potassium dihydrogen phosphate (KH_2PO_4), disodium hydrogen phosphate ($\text{Na}_2\text{HPO}_4 \cdot 12\text{H}_2\text{O}$), glutaraldehyde (GA), glucose, ascorbic acid, norfloxacin, uric acid, tenofovir, favipiravir, histidine, oxytetracycline were purchased from Sinopharm Chemical Reagent Co., Ltd (PR China) and used as received. Human IgG and bovine serum albumin (BSA) were purchased from Dingguo Changsheng Biotechnology Limited Company (PR China). The real saliva samples were collected from the Hefei University of Technology Hospital. Ultra-high pure water (conductivity 0.0548 $\mu\text{S}/\text{cm}$) was used in laboratory preparations.

High-resolution scanning electron microscopy (HRSEM) images of the samples were obtained by Regulus 8230 at an operating voltage of 15 kV (Hitachi Ltd., Japan). Transmission electron microscopy (TEM) micrographs were recorded on JEM-1400FLASH (JEOL, Japan). X-ray diffraction (XRD) patterns of the samples were recorded by Xpert PRO MPD (Nalytical, Netherlands). Magnetic measurement was carried out using an MPMS 3 vibrating sample magnetometer (Quantum Design, USA). The fourier-transform infrared spectroscopy (FTIR) technique was carried out using a Nicolet IS50 iN10 instrument (Thermo Nicolet, USA). Zeta potential was carried out using a Zetasizer Nano ZS-90 (Spectris, China). X-ray photoelectron spectroscopy (XPS) technique was used with an Escalab 250Xi instrument (Thermo, USA).

2.2. Preparation of $\text{Fe}_3\text{O}_4@/\text{SiO}_2$ -Au nanomaterials

2.2.1. Synthesis of Fe_3O_4 nanoparticles

The Fe_3O_4 nanoparticles were synthesized as described in Liu [30] with the following modifications. 2.025 g $\text{FeCl}_3 \cdot 6\text{H}_2\text{O}$ was dissolved in 60 mL ethylene glycol with stirring for 30 min, then 0.88 g $\text{C}_6\text{H}_5\text{Na}_3\text{O}_7 \cdot 2\text{H}_2\text{O}$ was

added and heated to 60 °C with stirring continued for 30 min. Finally, 9.84 g CH_3COONa were added to provide alkaline conditions enabling complete dissolution of the substrate. The dark yellow solution thus received was transferred to PTFE lined stainless-steel sealed container and autoclaved at 180 °C for 8 h. After cooling to room temperature, the substrate (Fe_3O_4) was magnetically separated and washed with ethanol and deionized water for three times each, then vacuum dried at 60 °C.

2.2.2. Synthesis of $\text{Fe}_3\text{O}_4@/\text{SiO}_2$ nanocomposites

Using the Stöber improvement method [31], 0.05 g Fe_3O_4 nanoparticles were dissolved in a mixture of ethanol (80 mL) and deionized water (16 mL), sonicated for 20 min. Subsequently, to this mixture ammonia solution (2 mL, 28 wt%) was added followed by the slow addition of TEOS (1 mL) and was kept stirring at room temperature for 6 h. The resultant substrate was magnetically recovered and washed with ethanol and deionized for three times each, then vacuum dried at 60 °C to yield $\text{Fe}_3\text{O}_4@/\text{SiO}_2$ nanocomposites.

2.2.3. Preparation of Au nanoparticles

Au nanoparticles were obtained by reducing $\text{HAuCl}_4 \cdot 4\text{H}_2\text{O}$ with sodium citrate [32]. Briefly, $\text{HAuCl}_4 \cdot 4\text{H}_2\text{O}$ (100 mL, 1 wt %) aqueous solution was heated at 100 °C and 10 mL 38.8 mM $\text{C}_6\text{H}_5\text{Na}_3\text{O}_7 \cdot 2\text{H}_2\text{O}$ was added into the stirred solution when it started boiling. Finally, the dark brown colored Au nanoparticles were obtained.

2.2.4. Synthesis of $\text{Fe}_3\text{O}_4@/\text{SiO}_2$ -Au nanocomposites

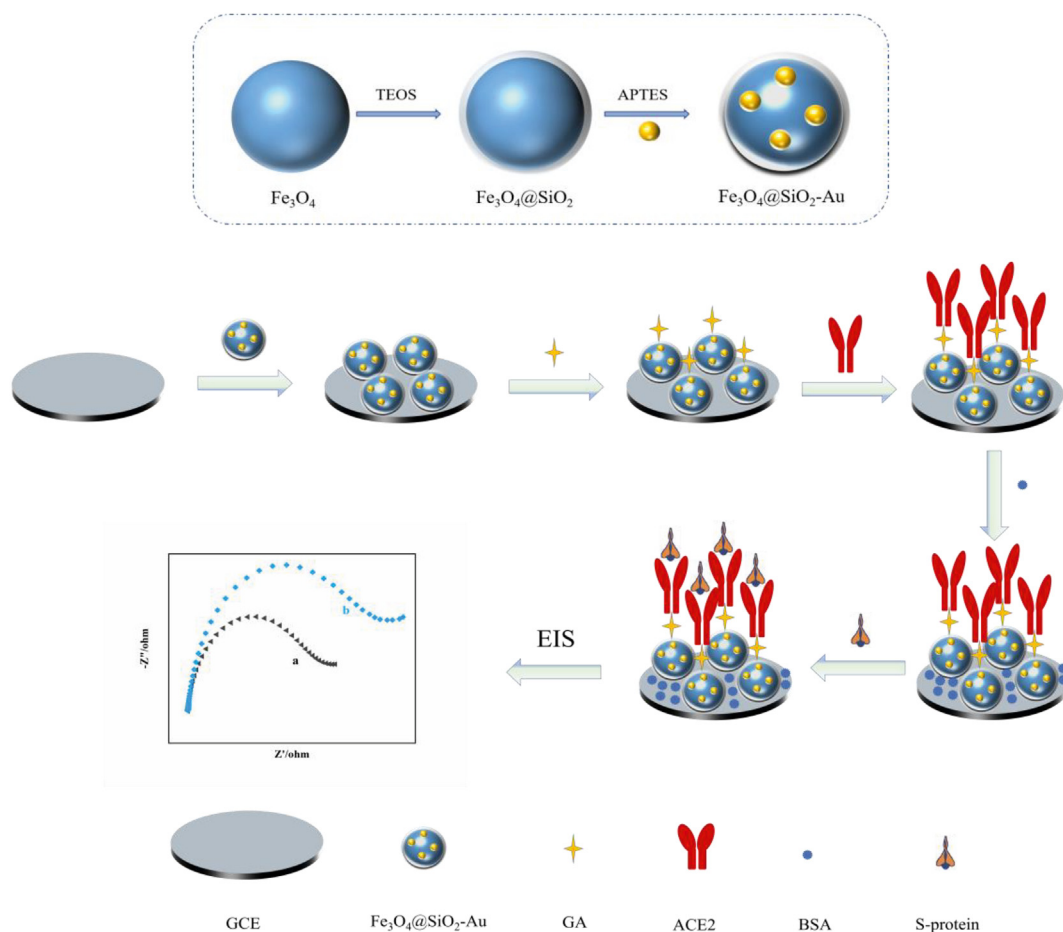
To functionalize $\text{Fe}_3\text{O}_4@/\text{SiO}_2$ with $-\text{NH}_2$ groups, 0.1 g $\text{Fe}_3\text{O}_4@/\text{SiO}_2$ was dispersed in ethanol (47.5 mL) and deionized water (2.5 mL) mixture followed by the addition of 0.4 mL APTES into the suspension with stirring for 4 h ($\text{Fe}_3\text{O}_4@/\text{SiO}_2-\text{NH}_2$). The $\text{Fe}_3\text{O}_4@/\text{SiO}_2-\text{NH}_2$ was re-dissolved in 40 mL deionized water, and then a certain amount of Au nanoparticles was added with stirring for 4 h. The resultant nanoparticles were magnetically separated and washed with ethanol and deionized water for three times each, then vacuum dried at 60 °C. In addition, the Au nanoparticles loading on $\text{Fe}_3\text{O}_4@/\text{SiO}_2$ composite were varied between 5 mL, 15 mL and 25 mL Au nanoparticles solution (hereafter designated as $\text{Fe}_3\text{O}_4@/\text{SiO}_2-\text{Au}_x$ where $x = 1, 2, 3$). Without special instructions, $\text{Fe}_3\text{O}_4@/\text{SiO}_2$ -Au nanocomposites synthesized from 15 mL Au nanoparticles were applied in the subsequent experiments.

2.3. Fabrication of S-protein electrochemical biosensor

The fabrication methodology of the chemically modified glassy carbon electrode (GCE) used for SARS-CoV-2 S-protein detection is shown in Scheme 1. The GCE was polished to a mirror surface using alumina powder with decreasing particle sizes: 1.0 μm , 0.3 μm , and 0.05 μm . Then the GCEs were ultrasonically cleaned with ethanol and ultrapure water for 3 min. Afterward, 6 μL of 3 mg/mL $\text{Fe}_3\text{O}_4@/\text{SiO}_2$ -Au suspension was added dropwise onto the electrode surface to obtain a chemically modified electrode, e.g., $\text{Fe}_3\text{O}_4@/\text{SiO}_2$ -Au/GCE. The $\text{Fe}_3\text{O}_4@/\text{SiO}_2$ -Au/GCE was then functionalized using glutaraldehyde (GA), ACE2, and bovine serum albumin (BSA). To modify with ACE2, the $\text{Fe}_3\text{O}_4@/\text{SiO}_2$ -Au/GCE surface was first functionalized with GA, then the receptor protein ACE2 was attached to the electrode surface at room temperature. Subsequently, the electrode surface was incubated using BSA prepared to block the possible binding sites of GA on the electrode surface (BSA/ACE2/GA/ $\text{Fe}_3\text{O}_4@/\text{SiO}_2$ -Au/GCE).

2.4. Characterizations of S-protein electrochemical biosensor

The binding of SARS-CoV-2 S-protein onto the electrochemical biosensor was attained by adding 6 μL S-protein solution on the BSA/ACE2/GA/ $\text{Fe}_3\text{O}_4@/\text{SiO}_2$ -Au/GCE surface and incubating at 37 °C for 30 min. The cyclic voltammetry (CV) curves and electrochemical impedance spectrograms (EIS) were obtained by a three-electrode



Scheme 1. Schematic illustration of the preparation process for $\text{Fe}_3\text{O}_4@\text{SiO}_2\text{-Au}$ and the fabrication of the electrochemical biosensor.

configuration, viz. chemically modified GCE, Ag/AgCl reference, and Pt counter electrodes, using 5.0 mM $[\text{Fe}(\text{CN})_6]^{3-/4-}$ in 0.1 M PBS with a pH 7.0 (Electrochemical station, CHI760E, China). The scan rate of the electrochemical analyzer was set at 100 mV/s in the CV experiments; EIS measurements were carried out in a frequency range of 0.1 Hz–100 kHz, with a signal amplitude (<10 mV) and open-circuit potential of 0.33 V. All experiments were performed at room temperature. The electrochemical impedance data was modeled with modified equivalent circuits using ZView software to estimate the charge transfer resistance under different experimental conditions. Finally, an electroanalytical method

was developed based on EIS for S-protein detection using the newly developed chemically modified $\text{Fe}_3\text{O}_4@\text{SiO}_2\text{-Au}$ electrode.

3. Results and discussion

3.1. Physical and chemical characterizations of the $\text{Fe}_3\text{O}_4@\text{SiO}_2\text{-Au}$ nanocomposite

Fig. 1 shows the morphology and micro-structures of Fe_3O_4 , $\text{Fe}_3\text{O}_4@\text{SiO}_2$, and $\text{Fe}_3\text{O}_4@\text{SiO}_2\text{-Au}$ nanomaterials observed through

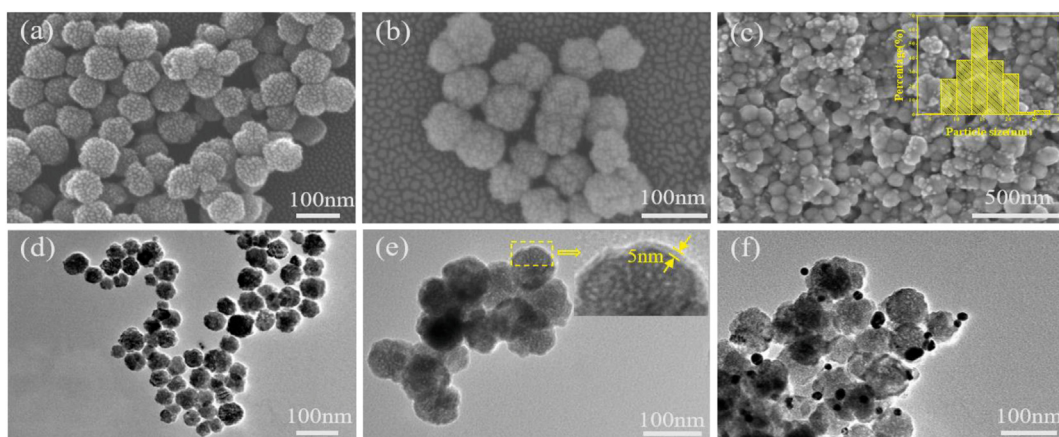


Fig. 1. Morphological characterization of nanomaterials: HRSEM images of (a) Fe_3O_4 , (b) $\text{Fe}_3\text{O}_4@\text{SiO}_2$, (c) $\text{Fe}_3\text{O}_4@\text{SiO}_2\text{-Au}$. TEM images of (d) Fe_3O_4 , (e) $\text{Fe}_3\text{O}_4@\text{SiO}_2$, (f) $\text{Fe}_3\text{O}_4@\text{SiO}_2\text{-Au}$.

HRSEM and TEM. Fe_3O_4 particulates tend to coagulate readily and citrate ligand was used to minimize coagulation [33]. As shown in Fig. 1a and d, Fe_3O_4 particulates are well-dispersed and spherical around the 60–70 nm size range. However, as shown in Fig. 1b, the $\text{Fe}_3\text{O}_4@/\text{SiO}_2$ nanocomposites are not well resolved to observe SiO_2 coating around Fe_3O_4 (except for some tonal variations). Therefore, the SiO_2 coating around the Fe_3O_4 forming a core-shell structure is shown in TEM analysis. The thickness of the SiO_2 layer is around 5 nm (Fig. 1e). The spread of Au nanoparticles around 15 nm average size on $\text{Fe}_3\text{O}_4@/\text{SiO}_2$ surface is visible in both SEM and TEM images. As shown in Fig. 1c and f, the Au nanoparticles are well-spread on the $\text{Fe}_3\text{O}_4@/\text{SiO}_2$ surface forming a large proportion of active sites to sequester ACE2 receptor protein.

The XRD diffractograms of Fe_3O_4 , $\text{Fe}_3\text{O}_4@/\text{SiO}_2$, and $\text{Fe}_3\text{O}_4@/\text{SiO}_2\text{-Au}$ nanomaterials are shown in Fig. 2a. The X-ray diffraction peaks of Fe_3O_4 at 2θ of 30.2° , 35.6° , 43.2° , 53.6° , 57.2° , and 62.7° , respectively are in agreement with spinel structure corresponding to (220), (311), (400), (422), (511), and (440) lattice planes (JCPDF:19-0629) [34,35]. In addition, the intensity of these diffraction peaks and the standard patterns are almost the same, indicating good Fe_3O_4 crystallinity. Further, the X-ray diffractograms of $\text{Fe}_3\text{O}_4@/\text{SiO}_2$ and Fe_3O_4 are also similar due to the amorphous nature of SiO_2 coating. The XRD data of $\text{Fe}_3\text{O}_4@/\text{SiO}_2\text{-Au}$ show the presence of Fe_3O_4 along (111) and (200) lattice planes of cubic Au nanoparticles corresponding to 2θ at 38.2° and 44.4° . The experimental data confirms further the successful incorporation of Au cubic nanocrystals on $\text{Fe}_3\text{O}_4@/\text{SiO}_2$ composites (hereafter $\text{Fe}_3\text{O}_4@/\text{SiO}_2\text{-Au}$).

The magnetic properties of Fe_3O_4 , $\text{Fe}_3\text{O}_4@/\text{SiO}_2$, and $\text{Fe}_3\text{O}_4@/\text{SiO}_2\text{-Au}$ nanomaterials are shown in Fig. 2b. The remanence and coercivity of material show their resistivity to demagnetization. Presently, all our nanomaterials observed zero remanence and coercivity values confirming their super magnetic properties. The B–H curves of $\text{Fe}_3\text{O}_4@/\text{SiO}_2$ and $\text{Fe}_3\text{O}_4@/\text{SiO}_2\text{-Au}$ are almost overlapped showing that the Au addition did not appreciably alter the magnetic strength of the composite. The magnetization intensity of Fe_3O_4 nanoparticles decreased from 87.67 emu/g to 39.18 emu/g and 37.61 emu/g upon sequential cladding with SiO_2 and Au doping, which confirms the successful synthesis of $\text{Fe}_3\text{O}_4@/\text{SiO}_2\text{-Au}$.

The FTIR spectra of Fe_3O_4 , $\text{Fe}_3\text{O}_4@/\text{SiO}_2$, and $\text{Fe}_3\text{O}_4@/\text{SiO}_2\text{-Au}$ nanomaterials are shown in Fig. 3a. The characteristic peaks detected at 1630 cm^{-1} and 3430 cm^{-1} are attributed to the stretching vibration of -OH , while the 799 cm^{-1} and 1090 cm^{-1} are ascribed due to Si–O stretching vibrations (this band is absent in Fe_3O_4). The IR bands at 576 cm^{-1} and 1400 cm^{-1} are specific to the stretching of Fe–O and -COOH , respectively [36]. Interestingly, the IR intensity of Fe–O bands decreases as $\text{Fe}_3\text{O}_4 > \text{Fe}_3\text{O}_4@/\text{SiO}_2 > \text{Fe}_3\text{O}_4@/\text{SiO}_2\text{-Au}$, which may be related to the coating of SiO_2 and doping of Au nanoparticles. Fig. 3b shows the zeta potential values of Fe_3O_4 , $\text{Fe}_3\text{O}_4@/\text{SiO}_2$, and $\text{Fe}_3\text{O}_4@/\text{SiO}_2\text{-Au}$ suspensions measured in pH 7.0. Bare Fe_3O_4 nanoparticles show a -4.11 mV zeta potential. After incorporating SiO_2 onto Fe_3O_4

nanoparticles, the surface becomes negatively charged due to the abundance of -OH offsets Fe–O charging. The negative zeta potential values show little agglomeration of $\text{Fe}_3\text{O}_4@/\text{SiO}_2$ nanocomposites. When APTES is used to functionalize $\text{Fe}_3\text{O}_4@/\text{SiO}_2$ sites a surface charge reversal occurred confirming the grafting of positively charged amino groups to the terminus of the substrates (viz., $\text{Fe}_3\text{O}_4@/\text{SiO}_2\text{-NH}_2$). The positively charged $\text{Fe}_3\text{O}_4@/\text{SiO}_2\text{-NH}_2$ sites adhere to Au nanoparticles readily again reversing the surface charge [37]. According to IR and zeta potential data, the -OH , -COOH , and -NH_2 groups abut from the $\text{Fe}_3\text{O}_4@/\text{SiO}_2\text{-Au}$ surface favor intimate interactions with receptor protein ACE2.

Fig. 4a shows the XPS survey spectra Fe_3O_4 , $\text{Fe}_3\text{O}_4@/\text{SiO}_2$, $\text{Fe}_3\text{O}_4@/\text{SiO}_2\text{-Au}$ nanomaterials, the presence of Fe, Si, Au, and associate valence states are confirmed. As shown in Fig. 4b, in all samples the deconvoluted peaks at 710.2 eV (Fe $2p_{1/2}$) and 723.6 eV (Fe $2p_{2/3}$) with a satellite confirming the presence of Fe^{2+} . Similarly, the peaks at 711.1 eV and 724.67 eV and the satellite show Fe^{3+} [38,39]. Moreover, the signatures of Fe 2p peaks do not vary which verifies the presence of Fe^{2+} and Fe^{3+} states [38,39]. The positions of the prominent Fe 2p peaks of the three substrates magnetic did not shift, which verifies that all Fe^{2+} and Fe^{3+} in all samples. As the XPS analysis was within 5 nm depth of the sample surface, the fluctuation of Fe 2p peaks during cladding and doping may be wide.

Fig. S1 shows the stability tests of three nanomaterials, confirming the contribution of SiO_2 coating to the stability of the nanocomposite coatings by comparing the changes in the redox peak currents of Fe_3O_4 , $\text{Fe}_3\text{O}_4@/\text{SiO}_2$, and $\text{Fe}_3\text{O}_4@/\text{SiO}_2\text{-Au}$ nanomaterials. The results conclude that $\text{Fe}_3\text{O}_4@/\text{SiO}_2\text{-Au}$ modified GCE is robust to the fabrication biosensor. Also shown in Fig. S1g and h, the oxidation peak current of the $\text{Fe}_3\text{O}_4@/\text{SiO}_2\text{-Au}$ nanomaterials modified electrode was reduced by 9.2% from day 1 to day 14. Therefore, all electrochemical biosensor data presented in this study were obtained using the newly modified electrode.

The cyclic voltametric curves (CV) obtained for $5.0\text{ mM } [\text{Fe}(\text{CN})_6]^{3-/4-}$ in 0.1 M PBS at pH 7.0 using bare and chemically modified GCE sensors are shown in Fig. S2. Always the CV curves show a symmetry due to the reversible nature of $\text{Fe}^{2+} \rightarrow \text{Fe}^{3+}$ electron transfer. The highest CV current peak is observed with $\text{Fe}_3\text{O}_4@/\text{SiO}_2\text{-Au}/\text{GCE}$ sensor due to the presence of Au nanoparticles (Fig. S2a). The current peak values decrease in order $\text{Fe}_3\text{O}_4@/\text{SiO}_2\text{-Au}/\text{GCE} > \text{Fe}_3\text{O}_4@/\text{SiO}_2/\text{GCE} > \text{bare GCE}$ showing the hindrance for electrons transfer due to the presence of SiO_2 . Fig. S2b shows the calibration curve to the peak current intensity with the square root of the scanning rate recorded for different nanomaterial-modified electrodes. The calculated electrochemically active surface area of bare GCE, $\text{Fe}_3\text{O}_4/\text{GCE}$, $\text{Fe}_3\text{O}_4@/\text{SiO}_2/\text{GCE}$, and $\text{Fe}_3\text{O}_4@/\text{SiO}_2\text{-Au}/\text{GCE}$ obtained by Randles-Sevcik formula [40] is 0.043 cm^2 , 0.055 cm^2 , 0.051 cm^2 and 0.060 cm^2 , respectively. The high electron transport capacity of Fe_3O_4 nanoparticles and Au nanoparticles can increase the

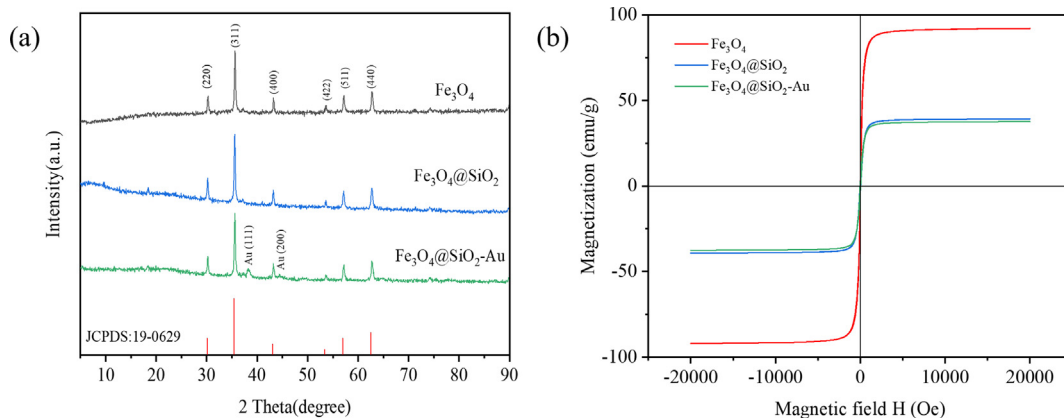


Fig. 2. (a) The XRD patterns and (b) magnetic hysteresis loops of Fe_3O_4 , $\text{Fe}_3\text{O}_4@/\text{SiO}_2$, $\text{Fe}_3\text{O}_4@/\text{SiO}_2\text{-Au}$.

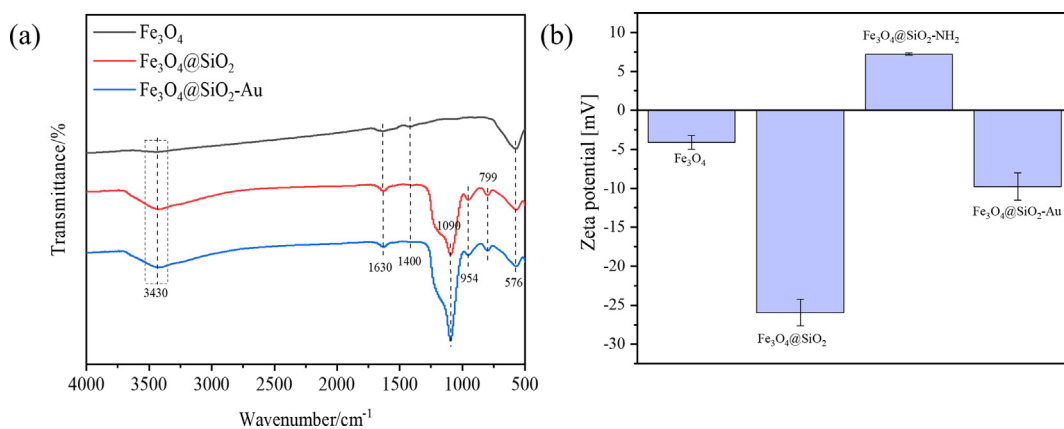


Fig. 3. (a) The FTIR spectra of Fe_3O_4 , $\text{Fe}_3\text{O}_4@SiO_2$, $\text{Fe}_3\text{O}_4@SiO_2-Au$. (b) The dynamic light scattering (DLS, Zeta potentials) of Fe_3O_4 , $\text{Fe}_3\text{O}_4@SiO_2$, $\text{Fe}_3\text{O}_4@SiO_2-NH_2$, $\text{Fe}_3\text{O}_4@SiO_2-Au$.

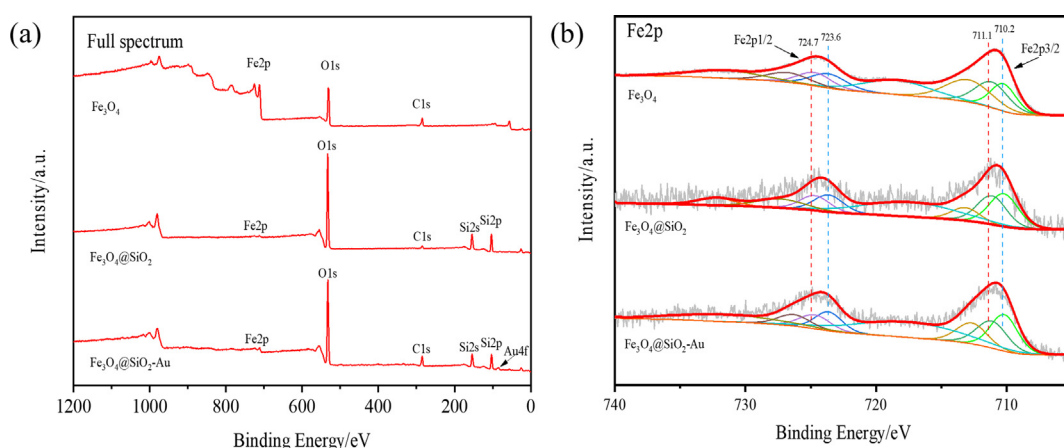


Fig. 4. (a) XPS full spectrum of $\text{Fe}_3\text{O}_4@SiO_2-Au$ materials. (b) Fe 2p energy spectrum of Fe_3O_4 , $\text{Fe}_3\text{O}_4@SiO_2$, and $\text{Fe}_3\text{O}_4@SiO_2-Au$.

electrochemically active area of the modified electrode, providing more electrochemically active sites for receptor protein ACE2 immobilization.

3.2. The electrochemical characterization of the biosensors

The as-fabricated electrochemical biosensor process was elucidated by CV and EIS in 5.0 mM $[\text{Fe}(\text{CN})_6]^{3-/4-}$ in 0.1 M PBS with a pH 7.0. As shown in Fig. 5a, after the modification of GCE by the $\text{Fe}_3\text{O}_4@SiO_2-Au$, the value of the redox current dramatically augmented compared to the GCE. This is due to the good electrochemical activity of $\text{Fe}_3\text{O}_4@SiO_2-Au$ which accelerates the electron transfer on the electrode surface. When

GA and the receptor protein ACE2 are immobilized on the modified electrode surface, the redox current significantly decreased due to the presence of cross-linked macromolecular structures in GA and the receptor protein ACE2, which prevented electron transfer. Moreover, when the BSA was used to block the non-specific active sites, the redox peak further decreased. The lowest redox peak for the S-protein was attributed to the tight binding of the S-protein and the receptor protein ACE2, which made the exchange reaction between electrons at the electrode surface more difficult. Fig. 5b shows Nyquist plots including semicircle (a measure of electron transfer rate) and linear (a measure of charge diffusion) segments representing high and low-frequency regions

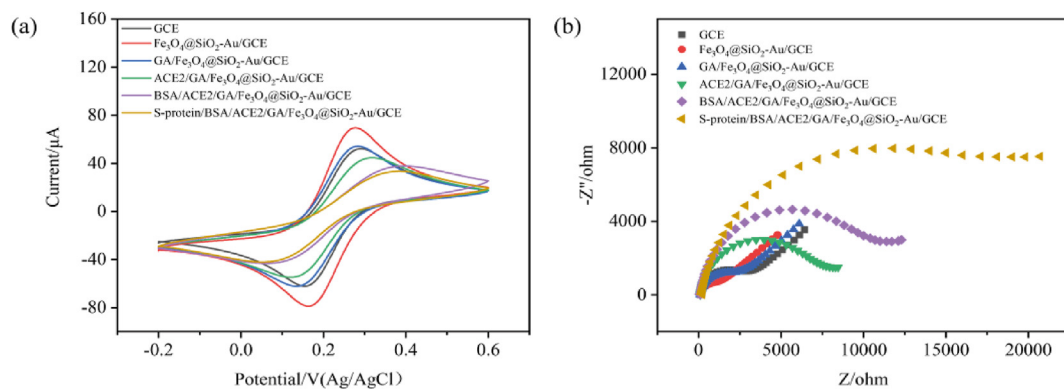


Fig. 5. The cyclic voltammograms (a) and Nyquist plots (b) representing the stepwise deposition of $\text{Fe}_3\text{O}_4@SiO_2-Au$ nanomaterials, glutaraldehyde (GA), receptor protein ACE2, bovine serum albumin (BSA) blocker, and 0.1 ng/mL SARS-CoV-2 S-protein.

[41–43]. The EIS measurements are in agreement with the CV data. The $\text{Fe}_3\text{O}_4@\text{SiO}_2\text{-Au}$ modified GCE had the smallest charge-transfer resistance (R_{ct}) compared to the bare GCE. When its surface was added with GA cross-linking, the R_{ct} increased. Especially, when ACE2, BSA, and S-protein were added on the electrode surface, the R_{ct} values increased orderly due to the non-conductive properties of these protein layers.

To evaluate the electrochemical reaction kinetics of SARS-CoV-2 S-protein at the BSA/ACE2/GA/ $\text{Fe}_3\text{O}_4@\text{SiO}_2\text{-Au}$ /GCE, different CV curves were measured in solutions containing $5.0\text{ mM } [\text{Fe}(\text{CN})_6]^{3-/4-}$ in 0.1 M PBS with a pH 7.0. The redox peak currents versus the square root of the scan rate curves (Fig. S3) indicate that the electron transfer process on as-fabricated electrochemical biosensor is diffusion-controlled [44].

3.3. $\text{Fe}_3\text{O}_4@\text{SiO}_2\text{-Au}$ /GCE sensor optimization

In order to obtain the best sensitivity of S-protein detection, the optimization experiments including the concentration of ACE2, the interaction temperature, and the interaction time of S-protein and ACE2 (Fig. 6). When the ACE2 is varied between 1 and $25\text{ }\mu\text{g/mL}$, the R_{ct} value was optimal at $20\text{ }\mu\text{g/mL}$ ACE2 and afterward, it shows a slight decline. The system temperature and time exert a significant impact on the biochemical activity of S-protein. As shown in Fig. 6b and c, optimal R_{ct} values were obtained at $37\text{ }^\circ\text{C}$ interaction temperature and 30 min interaction time. Interestingly it represents the average body temperature of humans. In subsequent studies, the following experimental conditions were used; $20\text{ }\mu\text{g/mL}$ ACE2 concentration, $37\text{ }^\circ\text{C}$ interaction temperature, and 30 min interaction time.

3.4. Detection performance of the S-protein electrochemical biosensor

A separate experiment was carried out to determine the performance of the $\text{Fe}_3\text{O}_4@\text{SiO}_2\text{-Au}$ /GCE biosensor for S-protein detection as a function of Au nanoparticles loading. In this experiment, the loading of

Au nanoparticles onto $\text{Fe}_3\text{O}_4@\text{SiO}_2$ was varied between 5 mL, 15 mL, 25 mL (Fig. S4). The GCE was then chemically modified using $\text{Fe}_3\text{O}_4@\text{SiO}_2\text{-Au}_x$ where x ranged from 1, 2, 3 ($\text{Fe}_3\text{O}_4@\text{SiO}_2\text{-Au}_x/\text{GCE}$). The S-protein detection performance obtained by $\text{Fe}_3\text{O}_4@\text{SiO}_2\text{-Au}_x/\text{GCE}$ sensor is shown in Fig. S5. Initially, the EIS response signal steadily increased with the Au nanoparticles loading showing an optimal value when $\text{Fe}_3\text{O}_4@\text{SiO}_2\text{-Au}_2/\text{GCE}$ sensor is used for measurements. At suitable Au nanoparticles loading, well-dispersed particulates yield an abundance of reactive sites for S-protein binding. When the Au nanoparticles loading further increased 25 mL, the reactivity of the $\text{Fe}_3\text{O}_4@\text{SiO}_2\text{-Au}_3/\text{GCE}$ to S-protein is somewhat hindered as a result of particulates agglomeration (Fig. S5f). Therefore, in optimizing the performance of biosensors for S-protein detection $\text{Fe}_3\text{O}_4@\text{SiO}_2\text{-Au}_2/\text{GCE}$ (designated as $\text{Fe}_3\text{O}_4@\text{SiO}_2\text{-Au}/\text{GCE}$) is used.

The EIS response signals of 0.1 ng/mL S-protein solution measured with $\text{Fe}_3\text{O}_4@\text{SiO}_2\text{-Au}/\text{GCE}$ biosensor were also simulated using a modified Randles equivalent circuit [45]. Fig. 7a shows the agreement between experimental observations and the modeled data. The modified Randles model was also used to interpret the Nyquist plots for a series of S-protein concentrations (0.1 ng/mL to $10\text{ }\mu\text{g/mL}$) (Fig. 7b). The calculated R_{ct} values show a linear dependence with the logarithmic S-protein concentration when the solution matrix conditions are matched.

The relationship between S-protein concentration as a function of ΔR_{ct} was estimated as $\Delta R_{ct} = 3605 \text{ Log } C + 12,121$ (limit of S-protein detection 4.78 ng/mL ; $R^2 = 0.991$) (Fig. 7c). The sensitivity and the linear dynamic range of the SARS-CoV-2 S-protein determination against our method are compared as shown in Table 1. The sensitivity and the linear dynamic range of S-protein detection depend on the nature of the sensors, and the electrochemical method used (for comparison, data obtained by molecular spectroscopic methods were also given). In terms of sensitivity and the linear dynamic range, the $\text{Fe}_3\text{O}_4@\text{SiO}_2\text{-Au}/\text{GCE}$ sensor developed presently shows the highest performance for S-protein detection by the EIS method.

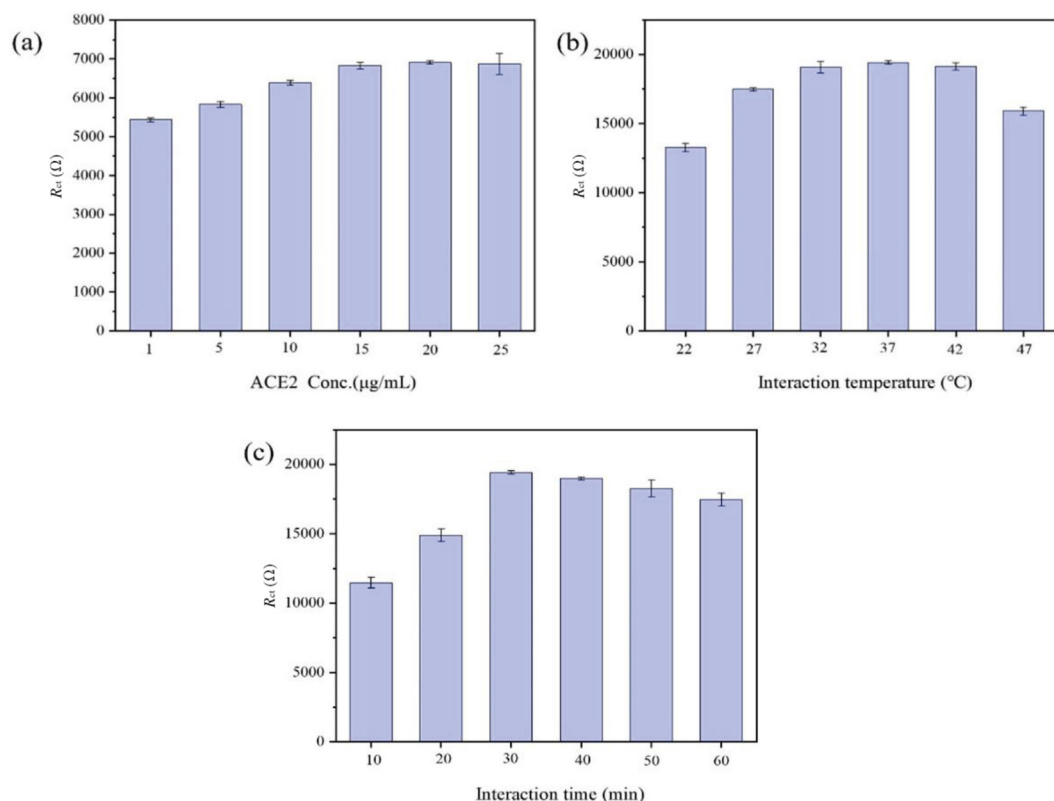


Fig. 6. The relationship between charge-transfer resistance signals and the concentration of ACE2 (a), the interaction temperature (b), and the interaction time (c) of S-protein and ACE2. Error bar = RSD ($n = 3$).

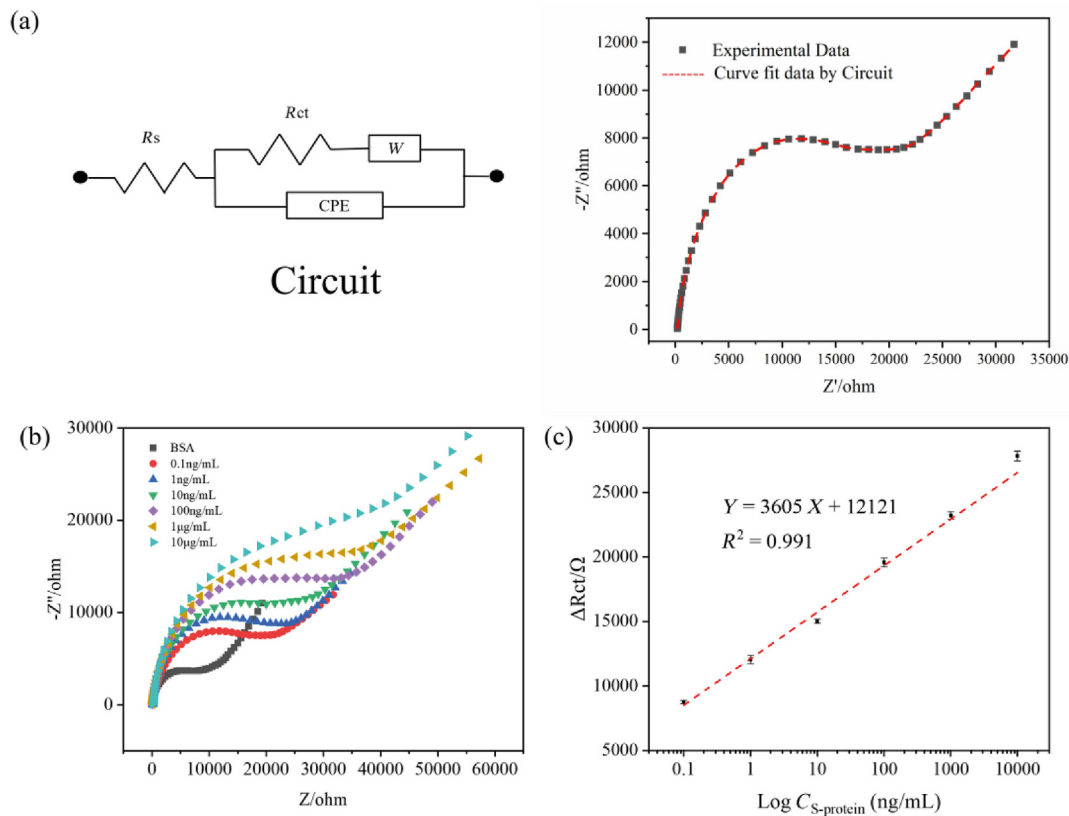


Fig. 7. (a) The modified Randles circuit with CPE element. R_s solution resistant; CPE, constant phase element; R_{ct} , charge transfer resistant; W , Warburg resistant. (b) Nyquist plots obtained $\text{Fe}_3\text{O}_4@/\text{SiO}_2\text{-Au}/\text{GCE}$ at various concentrations of SARS-CoV-2 S-protein and (c) the plot of logarithm concentrations against ΔR_{ct} .

Table 1

The comparison of the performance of biosensors constructed with different materials for the detection of SARS-CoV-2 S-protein.

Detection	Material	Linear range	LOD	Ref.
SERS	AuNPs	1–5 ng/mL	1 ng/mL	[46]
LIFA	AuNPs	0.1–1 ng/mL	0.1 ng/mL	[47]
Fluorescence	UCNPs@mSiO ₂	2–200 ng/mL	1.6 ng/mL	[48]
MPS	Fe ₃ O ₄	2.82–11.26 nM	1.56 nM	[49]
Colorimetric	Au@Pt	10–100 ng/mL	11 ng/mL	[50]
<i>I-t</i>	Co-TNTs	14–1400 nM	0.7 nM	[51]
DPV	SWCNT	0.3–300 nM	7 nM	[52]
LSV	CB/MB	0.04–10 µg/mL	19 ng/mL	[53]
SWV	MB	3.12–200 ng/mL	0.2 ng/mL	[54]
EIS	Fe ₃ O ₄ @SiO ₂ -Au	0.1–10 ⁴ ng/mL	4.78 pg/mL	This work

SERS, surface-enhanced Raman scattering; MPS, magnetic particle spectroscopy; EIS, electrochemical impedance spectroscopy; *I-t*, Amperometry; DPV, differential pulse voltammetry; LSV, linear sweep voltammetry; SWV, square wave voltammetry.

AuNPs, gold nanoparticles; UCNPs@mSiO₂, mesoporous silica encapsulated up-conversion nanoparticles; Co-TNTs, Co-functionalized TiO₂ nanotubes; SWCNT, single-walled carbon nanotube; CB, carbon black; MB, magnetic beads.

3.5. Selectivity, reproducibility, and repeatability

We examined the selectivity, repeatability, and reproductivity of $\text{Fe}_3\text{O}_4@/\text{SiO}_2\text{-Au}/\text{GCE}$ for the detection of S-protein by the EIS method using optimal experimental conditions developed in this study. In all these experiments 0.1 ng/mL S-protein solution was used. For selectivity analysis glucose, ascorbic acid, BSA, IgG, norfloxacin, uric acid, tenofovir, favipiravir, histidine, oxytetracycline were used as potential interferents. As shown in Fig. S6a, in the presence of these interferents, the S-protein in the solution can be detected with high selectivity (RSD < 4%). In evaluating the sensor reproduction, six identical $\text{Fe}_3\text{O}_4@/\text{SiO}_2\text{-Au}/\text{GCE}$

Table 2

Detection of S-protein in real saliva samples.

Samples	S-protein concentration (ng/mL)	Recovered (ng/mL)	Recovery (%)	RSD(%)
1	1	1.03	103	4.1
2	5	4.94	98.8	3.2
3	10	9.71	97.1	3.6
4	50	49.7	99.4	4.4
5	100	102	102	3.5

sensors were fabricated for S-protein measurements with good reproducibility (Fig. S6b; RSD < 1%). To determine the repeatability, a newly prepared $\text{Fe}_3\text{O}_4@/\text{SiO}_2\text{-Au}/\text{GCE}$ sensor was used for two consecutive weeks for measurements of S-protein concentration. The RSD value of S-protein detection was always less than 5% (Fig. S6c).

3.6. Detection of S-protein in saliva

The detection of SARS-CoV-2 S-protein in saliva using $\text{Fe}_3\text{O}_4@/\text{SiO}_2\text{-Au}/\text{GCE}$ biosensor was also carried out by multiple standard addition method. The filtered and diluted saliva sample was spiked with S-protein at varying concentrations between 1 and 100 ng/mL, and the final analyte concentration was determined in triplicate by EIS; the results thus obtained are given in Table 2. The spiked recovery of S-protein in the saliva is always above 97% and the relative standard deviation is below 5%. The results indicate the suitability of $\text{Fe}_3\text{O}_4@/\text{SiO}_2\text{-Au}/\text{GCE}$ biosensor in detecting SARS-CoV-2 S-protein in saliva with high precision and accuracy.

4. Conclusions

Preventing the spread of the SARS-CoV-2 virus and its variants requires the development of a rapid and cost-effective detection method.

To our knowledge for the first time, we developed an electrochemical sensor by chemically modifying a GCE with $\text{Fe}_3\text{O}_4@\text{SiO}_2\text{-Au}$ ($\text{Fe}_3\text{O}_4@\text{SiO}_2\text{-Au/GCE}$) for rapid detection of SARS-CoV-2 S-protein with a wide dynamic range (0.1 ng/mL to 10 $\mu\text{g/mL}$) and low limit detection (4.78 pg/mL). The new electrochemical sensor shows robust behavior with excellent stability and reproducibility for S-protein detection. Moreover, the sensor could ultimately lead to corresponding determination in real samples. Once a miniaturized module of the electrochemical sensor is fabricated (currently in progress), it holds promise as a sensitive screening method to combat the SARS-CoV-2 global endemic.

Declaration of competing interest

The authors declare that they have no known competing financial interests or personal relationships that could have appeared to influence the work reported in this paper.

Acknowledgments

The authors acknowledge the financial support from the National Key Research and Development Program of China (2022YFE0110100), Key Science and Technology Projects of Anhui Province (202003a07020004), and National Natural Science Foundation of China (21777164). Program of Distinguished Professor in B & R Countries (DL20180052) abidance at the Hefei University of Technology.

Appendix A. Supplementary data

Supplementary data to this article can be found online at <https://doi.org/10.1016/j.asems.2023.100067>.

References

- M. Cevik, M. Tate, O. Lloyd, A.E. Maraolo, J. Schafers, A. Ho, SARS-CoV-2, SARS-CoV, and MERS-CoV viral load dynamics, duration of viral shedding, and infectiousness: a systematic review and meta-analysis, *Lancet Microbe* 2 (2021) 13–22, [https://doi.org/10.1016/s2666-5247\(20\)30172-5](https://doi.org/10.1016/s2666-5247(20)30172-5).
- K. Dhama, S. Khan, R. Tiwari, S. Sircar, S. Bhat, Y.S. Malik, K.P. Singh, W. Chaicumpa, D.K. Bonilla-Aldana, A.J. Rodriguez-Morales, Coronavirus disease 2019-COVID-19, *Clin. Microbiol. Rev.* 33 (2020) 288, <https://doi.org/10.1128/cmr.00028-20>, 20.
- R. Antiochia, Nanobiosensors as new diagnostic tools for SARS, MERS and COVID-19: from past to perspectives, *Microchim. Acta* 187 (2020) 639, <https://doi.org/10.1007/s00604-020-04615-x>.
- Y.W. Tang, J.E. Schmitz, D.H. Persing, C.W. Stratton, Laboratory diagnosis of COVID-19: current issues and challenges, *J. Clin. Microbiol.* 58 (2020) e00512–e00520, <https://doi.org/10.1128/jcm.00512-20>.
- M. Li, F.F. Yin, L. Song, X.H. Mao, F. Li, C.H. Fan, X.L. Zuo, Q. Xia, Nucleic acid tests for clinical translation, *Chem. Rev.* 121 (2021) 10469–10558, <https://doi.org/10.1021/acs.chemrev.1c00241>.
- D.C. Lin, L. Liu, M.X. Zhang, Y.L. Hu, Q.T. Yang, J.B. Guo, Y.C. Dai, Y.Z. Xu, Y. Cai, X.C. Chen, K.S. Huang, Z. Zhang, Evaluations of the serological test in the diagnosis of 2019 novel coronavirus (SARS-CoV-2) infections during the COVID-19 outbreak, *Eur. J. Clin. Microbiol. Infect. Dis.* 39 (2020) 2271–2277, <https://doi.org/10.1007/s10096-020-03978-6>.
- Y. Dang, N. Liu, C.A.R. Tan, Y.M. Feng, X.X. Yuan, D.D. Fan, Y.K. Peng, R.H. Jin, Y. Guo, J.L. Lou, Comparison of qualitative and quantitative analyses of COVID-19 clinical samples, *Clin. Chim. Acta* 510 (2020) 613–616, <https://doi.org/10.1016/j.cca.2020.08.033>.
- Z. Abusrewil, I.M. Alhudiri, H.H. Kaal, S.E. El Meshri, F.O. Ebrahim, T. Dalyoum, A.A. Efrefer, K. Ibrahim, M.B. Elfghi, S. Abusrewil, A. Elzagheid, Time scale performance of rapid antigen testing for SARS-CoV-2: evaluation of 10 rapid antigen assays, *J. Med. Virol.* 93 (2021) 6512–6518, <https://doi.org/10.1002/jmv.27186>.
- Z.H. Chen, Z.G. Zhang, X.M. Zhai, Y.Y. Li, L. Lin, H. Zhao, L. Bian, P. Li, L. Yu, Y.S. Wu, G.F. Lin, Rapid and sensitive detection of anti-SARS-CoV-2 IgG, using lanthanide-doped nanoparticles-based lateral flow immunoassay, *Anal. Chem.* 92 (2020) 7226–7231, <https://doi.org/10.1021/acs.analchem.0c00784>.
- X. Pan, A.C. Kaminga, Y. Chen, H. Liu, S.W. Wen, Y. Fang, P. Jia, A. Liu, Auxiliary screening COVID-19 by serology, *Front. Public Health* 10 (2022), <https://doi.org/10.3389/fpubh.2022.819841>.
- B. Li, A.M. Yu, G.S. Lai, Self-assembly of phenoxyl-dextran on electrochemically reduced graphene oxide for nonenzymatic biosensing of glucose, *Carbon* 127 (2018) 202–208, <https://doi.org/10.1016/j.carbon.2017.10.096>.
- M. Negahdary, L. Angnes, Electrochemical aptamer-based nanobiosensors for diagnosing Alzheimer's disease: a review, *Biomater. Adv.* 135 (2022), 112689, <https://doi.org/10.1016/j.msec.2022.112689>.
- L.J. Lei, B. Ma, C.T. Xu, H. Liu, Emerging tumor-on-chips with electrochemical biosensors, *Trac-Trends Anal. Chem.* 153 (2022), 116640, <https://doi.org/10.1016/j.trac.2022.116640>.
- T. Chaibun, J. Puenpa, T. Ngamdee, N. Boonapatcharoen, P. Athamanolap, A.P. O'Mullane, S. Vongpunsawad, Y. Poovorawan, S.Y. Lee, B. Lertanantawong, Rapid electrochemical detection of coronavirus SARS-CoV-2, *Nat. Commun.* 12 (2021) 802, <https://doi.org/10.1038/s41467-021-21121-7>.
- J. Kudr, P. Michalek, L. Ilieva, V. Adam, O. Zitka, COVID-19: a challenge for electrochemical biosensors, *Trac, Trends Anal. Chem.* 136 (2021), 116192, <https://doi.org/10.1016/j.trac.2021.116192>.
- V.V. Tran, N.H.T. Tran, H.S. Hwang, M. Chang, Development strategies of conducting polymer-based electrochemical biosensors for virus biomarkers: potential for rapid COVID-19 detection, *Biosens. Bioelectron.* 182 (2021) 540–552, <https://doi.org/10.1016/j.bios.2021.113192>.
- A. Gb, B. Aha, A. Ma, B. Np, C. Ss, E. Ptad, Emerging materials for the electrochemical detection of COVID-19, *J. Electroanal. Chem.* 893 (2021), 115289, <https://doi.org/10.1016/j.jelechem.2021.115289>.
- M. Elbadawi, J.J. Ong, T.D. Pollard, S. Gaisford, A.W. Basit, Additive manufacturable materials for electrochemical biosensor electrodes, *Adv. Funct. Mater.* 31 (2021), 2006407, <https://doi.org/10.1002/adfm.202006407>.
- A.L. Lorenzen, A.M. Dos Santos, L.P. Dos Santos, L. da Silva Pinto, F.R. Conceicao, F. Wolfart, PEDOT-AuNPs-based impedimetric immunosensor for the detection of SARS-CoV-2 antibodies, *Electrochim. Acta* 404 (2022), 139757, <https://doi.org/10.1016/j.electacta.2021.139757>, 139757.
- M.A. Ali, C. Hui, S. Jahan, B. Yuan, M.S. Saleh, E. Ju, S.-J. Gao, R. Panat, Sensing of COVID-19 antibodies in seconds via aerosol jet nanoprinted reduced-graphene-oxide-coated 3D electrodes, *Adv. Mater.* 33 (2021), 2006647, <https://doi.org/10.1002/adma.202006647>.
- R. Torrente-Rodríguez, H. Lukas, J. Tu, J. Min, Y. Yang, C. Xu, H.B. Rossiter, W. Gao, SARS-CoV-2 RapidPlex: a graphene-based multiplexed telemedicine platform for rapid and low-cost COVID-19 diagnosis and monitoring, *Matter* 3 (2020) 1981–1998, <https://doi.org/10.1016/j.matt.2020.09.027>.
- F. Haghayegh, R. Salahandish, M. Hassani, A. Sanatnezhad, Highly stable buffer-based zinc oxide/reduced graphene oxide nanosurface chemistry for rapid immunosensing of SARS-CoV-2 antigens, *ACS Appl. Mater. Interfaces* 14 (2022) 10844–10855, <https://doi.org/10.1021/acsami.1c24475>.
- H.V. Tran, N.M. Ngo, R. Medhi, P. Srinoi, T.T. Liu, S. Rittikulsittichai, T.R. Lee, Multifunctional iron oxide magnetic nanoparticles for biomedical applications: a review, *Materials* 15 (2022) 503, <https://doi.org/10.3390/ma15020503>.
- N. Sanaeifar, M. Rabiee, M. Abdolrahim, M. Tahriri, D. Vashae, L. Tayebi, A novel electrochemical biosensor based on Fe_3O_4 nanoparticles-polyvinyl alcohol composite for sensitive detection of glucose, *Anal. Biochem.* 519 (2017) 19–26, <https://doi.org/10.1016/j.ab.2016.12.006>.
- X.N. Liu, F.H. Zhu, W. Wang, J.H. Lei, G.F. Yin, Synthesis of single-crystalline iron oxide magnetic nanorings as electrochemical biosensor for dopamine detection, *Int. J. Electrochem. Sci.* 11 (2016) 9696–9703, <https://doi.org/10.20964/2016.11.62>.
- R. Antiochia, Electrochemical biosensors for SARS-CoV-2 detection: voltametric or impedimetric transduction? *Bioelectrochemistry* 147 (2022), 108190 <https://doi.org/10.1016/j.bioelechem.2022.108190>.
- M. Torres, W. Araujo, L. Lima, A.L. Ferreira, C. Fuente-Nunez, Low-cost biosensor for rapid detection of SARS-CoV-2 at the point of care, *Matter* 4 (2021) 2403–2416, <https://doi.org/10.1016/j.matt.2021.05.003>.
- Y.T. Buyuksunetci, B.E. Cital, U. Anik, An impedimetric approach for COVID-19 detection, *Analyst* 147 (2021) 130–138, <https://doi.org/10.1039/d1an01718g>.
- Z. Lukacs, T. Kristof, A generalized model of the equivalent circuits in the electrochemical impedance spectroscopy, *Electrochim. Acta* 363 (2020), <https://doi.org/10.1016/j.electacta.2020.137199>.
- J. Liu, Z.K. Sun, Y.H. Deng, Y. Zou, C.Y. Li, X.H. Guo, L.Q. Xiong, Y. Gao, F.Y. Li, D.Y. Zhao, Highly water-dispersible biocompatible magnetite particles with low cytotoxicity stabilized by citrate groups, *Angew. Chem. Int. Ed.* 48 (2009) 5875–5879, <https://doi.org/10.1002/anie.200901566>.
- C. Hui, C.M. Shen, J.F. Tian, L.H. Bao, H. Ding, C. Li, Y.A. Tian, X.Z. Shi, H.J. Gao, Core-shell $\text{Fe}_3\text{O}_4@\text{SiO}_2$ nanoparticles synthesized with well-dispersed hydrophilic Fe_3O_4 seeds, *Nanoscale* 3 (2011) 701–705, <https://doi.org/10.1039/c0nr00497a>.
- K.R. Brown, A.P. Fox, M.J. Natan, Morphology-dependent electrochemistry of cytochrome c at Au colloid-modified SnO_2 electrodes, *J. Am. Chem. Soc.* 118 (1996) 1154–1157, <https://doi.org/10.1021/ja952951w>.
- H. Deng, X.L. Li, Q. Peng, X. Wang, J.P. Chen, Y.D. Li, Monodisperse magnetic single-crystal ferrite microspheres, *Angew. Chem. Int. Ed.* 44 (2005) 2782–2785, <https://doi.org/10.1002/anie.200462551>.
- Q. Zhang, R. Chen, J.Y. Gong, M. Yuan, L.Y. Chen, Single-crystalline Fe_3O_4 nanosheets: facile sonochemical synthesis, evaluation and magnetic properties, *J. Alloys Compd.* 577 (2013) 528–532, <https://doi.org/10.1016/j.jallcom.2013.06.176>.
- W. Zhang, F.L. Shen, R.Y. Hong, Solvothermal synthesis of magnetic Fe_3O_4 microparticles via self-assembly of Fe_3O_4 nanoparticles, *Particuology* 9 (2011) 179–186, <https://doi.org/10.1016/j.partic.2010.07.025>.
- N. Shahabadi, M. Falsafi, K. Mansouri, Improving antiproliferative effect of the anticancer drug cytarabine on human promyelocytic leukemia cells by coating on $\text{Fe}_3\text{O}_4@\text{SiO}_2$ nanoparticles, *Colloid. Surfaces B-Biointerfaces* 141 (2016) 213–222, <https://doi.org/10.1016/j.colsurfb.2016.01.054>.

- [37] M.E. Khosroshahi, L. Ghazanfari, Physicochemical characterization of Fe₃O₄/SiO₂/Au multilayer nanostructure, *Mater. Chem. Phys.* 133 (2012) 55–62, <https://doi.org/10.1016/j.matchemphys.2011.12.047>.
- [38] T. Radu, A. Petran, D. Olteanu, I. Baldea, M. Potara, R. Turcu, Evaluation of physicochemical properties and biocompatibility of new surface functionalized Fe₃O₄ clusters of nanoparticles, *Appl. Surf. Sci.* 501 (2020), 144267, <https://doi.org/10.1016/j.apsusc.2019.144267>.
- [39] M.C. Biesinger, B.P. Payne, A.P. Grosvenor, L.W.M. Lau, A.R. Gerson, R.S. Smart, Resolving surface chemical states in XPS analysis of first row transition metals, oxides and hydroxides: Cr, Mn, Fe, Co and Ni, *Appl. Surf. Sci.* 257 (2011) 2717–2730, <https://doi.org/10.1016/j.apsusc.2010.10.051>.
- [40] T. Paixao, Measuring electrochemical surface area of nanomaterials versus Randles-Sevcik equation, *Chemelectrochem* 7 (2020) 3414–3415, <https://doi.org/10.1002/celec.202000633>.
- [41] V. Vivier, M.E. Orazem, Impedance analysis of electrochemical systems, *Chem. Rev.* 122 (2022) 11131–11168, <https://doi.org/10.1021/acs.chemrev.1c00876>.
- [42] O. Gharbi, M.T.T. Tran, B. Tribollet, M. Turmine, V. Vivier, Revisiting cyclic voltammetry and electrochemical impedance spectroscopy analysis for capacitance measurements, *Electrochim. Acta* 343 (2020), 136109, <https://doi.org/10.1016/j.electacta.2020.136109>.
- [43] C.M.A. Brett, Electrochemical impedance spectroscopy in the characterisation and application of modified electrodes for electrochemical sensors and biosensors, *Molecules* 27 (2022) 1497, <https://doi.org/10.3390/molecules27051497>.
- [44] M. Mehmandoust, S. Cakar, M. Ozacar, N. Erk, The determination of timolol maleate using silver/tannic acid/titanium oxide nanocomposite as an electrochemical sensor in real samples, *Electroanalysis* 34 (2022) 1150–1162, <https://doi.org/10.1002/elan.202100363>.
- [45] R. Saxena, S. Srivastava, An insight into impedimetric immunosensor and its electrical equivalent circuit, *Sens. Actuat. B-Chem.* 297 (2019), 126780, <https://doi.org/10.1016/j.snb.2019.126780>.
- [46] A. Pramanik, Y. Gao, S. Patibandla, D. Mitra, P.C. Ray, Rapid diagnosis and effective inhibition of Corona virus using spike antibody attached gold nanoparticle, *Nanoscale Adv.* 3 (2021) 1588–1596, <https://doi.org/10.1039/d0na01007c>.
- [47] K.V. Serebrennikova, N.A. Byzova, A.V. Zherdev, N.G. Khlebtsov, B.N. Khlebtsov, S.F. Biketov, B.B. Dzantiev, Lateral flow immunoassay of SARS-CoV-2 antigen with SERS-based registration: development and comparison with traditional immunoassays, *Biosensors* 11 (2021) 510, <https://doi.org/10.3390/bios11120510>.
- [48] J. Guo, 5G-Enabled Ultra-sensitive Fluorescence Sensor for Proactive Prognosis of COVID-19, *Biosensors & Bioelectronics*, 2020, 113160, <https://doi.org/10.1016/j.bios.2021.113160>.
- [49] K. Wu, V.K. Chugh, V.D. Krishna, A.D. Girolamo, Y.A. Wang, R. Saha, S. Liang, C.J. Cheeran, J.P. Wang, One-step, wash-free, nanoparticle clustering-based magnetic particle spectroscopy (MPS) bioassay method for detection of SARS-CoV-2 spike and nucleocapsid proteins in liquid phase, *ACS Appl. Mater. Interfaces* 13 (2021) 44136–44146, <https://doi.org/10.1021/acsami.1c14657>.
- [50] Z. Fu, W. Zeng, S. Cai, H. Li, R. Yang, Porous Au@Pt nanoparticles with superior peroxidase-like activity for colorimetric detection of spike protein of SARS-CoV-2, *J. Colloid Interface Sci.* 604 (2021) 113–121, <https://doi.org/10.1016/j.jcis.2021.06.170>.
- [51] B.S. Vadlamani, T. Uppal, S.C. Verma, M. Misra, Functionalized TiO₂ nanotube-based electrochemical biosensor for rapid detection of SARS-CoV-2, *Sensors* 20 (2020) 5871, <https://doi.org/10.1101/2020.09.07.20190173>.
- [52] F. Curti, S. Fortunati, W. Knoll, M. Giannetto, R. Corradini, A. Bertucci, M. Careri, A folding-based electrochemical aptasensor for the single-step detection of the SARS-CoV-2 spike protein, *ACS Appl. Mater. Interfaces* 14 (2022) 19204–19211, <https://doi.org/10.1021/acsami.2c02405>.
- [53] L. Fabiani, M. Saroglia, G. Galatà, R.D. Santis, F. Arduini, Magnetic beads combined with carbon black-based screen-printed electrodes for COVID-19: a reliable and miniaturized electrochemical immunosensor for SARS-CoV-2 detection in saliva, *Biosens. Bioelectron.* 171 (2021), 112686, <https://doi.org/10.1016/j.bios.2020.112686>.
- [54] P. Malla, H.P. Liao, C.H. Liu, W.C. Wu, P. Sreearunothai, Voltammetric biosensor for coronavirus spike protein using magnetic bead and screen-printed electrode for point-of-care diagnostics, *Microchim. Acta* 189 (2022) 168, <https://doi.org/10.1016/j.bios.2020.112686>.